Systematic computational screening and design of double perovskites Q_2LiMH_6 (Q = K, Rb; M = Ga, In, Tl) for efficient hydrogen storage: A DFT and AIMD approach

Asif Hosen [a,*] , Ahmad A. Mousa [b], Ebrahim Nemati-Kande [c], Asif Nawaz Khan [d], Mohammed S. Abu-Jafar [e], Enrico Benassi [f], E.A. Elghmaz [g], N.S. Abd EL-Gawaad [h,*], Jihad Asad [i]

[a] Department of Materials Science and Engineering, Khulna University of Engineering & Technology (KUET), Khulna 9203, Bangladesh
[b] Middle East University, Amman 11831, Jordan
[c] Department of Physical Chemistry, Chemistry Faculty, Urmia University, Urmia, Iran
[d] Material Modeling and Simulation Lab, Department of Physics, University of Science & Technology, Bannu, 28100 Khyber Pakhtunkhwa, Pakistan
[e] Department of Physics, An-Najah National University, Nablus, Palestine
[f] Department of Physics, Informatics and Mathematics, University of Modena and Reggio Emilia, via Giuseppe Campi 213/B, 41125 Modena, Italy
[g] Department of Physics, King Khalid University, Abha 61421, Saudi Arabia
[h] Muhayil Asir, Applied College, King Khalid University, Abha 62529, Saudi Arabia
[i] Dep. of Physics, Faculty of applied Science, Palestine Technical University- Kadoorie, Tukarem P 305, Palestine

ARTICLE INFO

ABSTRACT

The development of efficient hydrogen storage solutions is crucial for advancing the commercialization of hydrogen-based energy systems. Solid-state hydrogen storage is emerging as a highly promising method, attracting considerable interest and necessitating in-depth research efforts. This study systematically designs six novel solid-state hydrides: K_2LiGaH_6, K_2LiInH_6, K_2LiTlH_6, Rb_2LiGaH_6, Rb_2LiInH_6, and Rb_2LiTlH_6, using density functional theory (DFT). The objective is to thoroughly investigate their structural, elastic, opto-electronic, thermodynamic, and hydrogen storage characteristics. The dynamical stability was analyzed, and the resulting phonon dispersion curves confirm that these materials are stable. Furthermore, ab initio molecular dynamics (AIMD) simulations confirm the thermal stability of the hydrides at room temperature (300 K), as no structural deformation was observed. The band structure indicates that all materials exhibit indirect band gap semiconducting behavior, with band gap values spanning from 0.3 to 2 eV. Optical property analysis reveals that these hydrides are effective ultraviolet absorbers, with a noticeable red shift in the absorption edge can be observed resulting from the variations of bandgap. All the hydrides demonstrate mechanical stability and exhibit brittle characteristics. The calculated gravimetric hydrogen storage capacities indicate that K_2LiGaH_6 has the highest capacity at 3.22 wt%, followed by K_2LiInH_6 (2.60 wt%), Rb_2LiGaH_6 (2.16 wt%), K_2LiTlH_6 (1.88 wt%), and Rb_2LiInH_6 (1.86 wt%), with Rb_2LiTlH_6 having the lowest value at 1.46 wt%. A decrease in storage capacity is observed when the cationic atom at the Q and M site in Q_2LiMH_6 is replaced, due to differences in atomic radius. Overall, the findings of this study identify Q_2LiMH_6 (Q = K, Rb; M = Ga, In, Tl) as a viable candidate for next-generation hydrogen storage owing to its optimal gravimetric capacity and excellent stability.

1. Introduction

One of the greatest challenges faced by technologists and scientists in the 21st century is ensuring a reliable global energy supply. The global energy sector is confronting major challenges such as population growth, industrialization, and rising living standards drive higher energy demand and substantial carbon output linked to fossil fuel usage. In 2008, global energy consumption reached 15 TW, and with the increasing population and industrial production, it is projected to nearly double by 2050 [1]. However, the majority of our energy supply still

---

comes from finite and non-renewable energy sources including coal, petroleum, and natural gas. Moreover, combustion of these non-renewable resources has led to severe ecological problems, such as contamination of air and water, alongside the escalating crisis of global warming. Given key factors such as the economy, environment, and human health, the rising energy demand must be met through renewable and sustainable sources. In this context, the decline of fossil fuel resources has spurred significant research into hydrogen (H_2) as a sustainable energy solution for the era beyond fossil fuels. So, there is widespread consensus that H_2 could be the potential candidate for tackling the triple challenges of economy, environment, and human health. With a calorific value between 120 and 142 MJ/kg, hydrogen offers the greatest energy-to-mass ratio of any traditional fuel, ranking second in overall energy content [2]. H_2 is regarded as a promising key energy source for the next generation, as it is non-toxic and capable of generating substantial power from natural sources like sunlight and water− both are clean, sustainable, and renewable. Therefore, it is now regarded as the primary energy solution and a versatile industrial resource, owing to its significant role in fostering a greener and more eco-friendly future for humanity [3].

In contrast to fossil fuels, hydrogen does not exist freely in the environment. However, hydrogen can be generated from a variety of primary energy sources and utilized as fuel, either by burning it in internal combustion engines or through conversion in fuel cells [4–7]. Once H_2 is generated, it is possible to store it in the form of gas, liquid, or absorbed into a solid material. Although, all three storage methods have its benefits, storing hydrogen as a gas requires highly pressurized containers, which are expensive, while storing it as a liquid necessitates cooling it to an extremely low temperature of 20 K [8]. To address these challenges, researchers have focused on solid-state hydrogen storage techniques, which meet essential criteria such as cost-effectiveness, safety, mass, and power density for the viable application of hydrogen technologies [9]. Research on solid-state hydrogen storage primarily emphasize carbonaceous substances, metallic hydrides, and advanced hydride compounds [10–14]. Hydrogen retention in carbon-based substances occurs via physisorption, which necessitates a substantial pore volume to achieve efficient absorption. However, even though their pore dimensions are comparatively limited, carbon nanotubes exhibit high H_2 storage densities [11]. Metallic hydrides form strong bonds with hydrogen, requiring elevated temperatures of approximately 120–200°C to effectively release their stored hydrogen [15]. Metal hydrides, such as MgH_2 and LiH, are widely recognized for their hydrogen storage capability, offering a gravimetric hydrogen density (GHD) of 5–8 wt% [15]. However, these hydrides face challenges due to their high

thermodynamic stability and sluggish kinetics [16]. Furthermore, $NaAlH_4$ [17–20], AlH_3 [21], $Mg(BH_4)_2$ [22], and $NaBH_4$ [23] are the hydrides that have met the 9 wt% gravimetric hydrogen storage targets set by the U.S. Department of Energy for 2015 [24–26]. Mg_2NiH_4 has garnered significant interest as a potential H_2 fuel due to its notable storage capacity, cost-effectiveness, low density, minimal toxicity, and distinctive structural and bonding features [27,28].

Recently, perovskite hydride materials have gained significant interest in the scientific community as potential options for hydrogen economy, owing to their remarkable gravimetric storage capacities. Perovskite-type hydrides are capable of absorbing and retaining hydrogen either at their surfaces or within their crystal lattices [29]. This makes them a promising candidate for overcoming the challenges related to the storage and transportation of gaseous H_2. Xu et al. [30] investigated titanium-based hydride perovskites, reporting moderate gravimetric storage densities of 3.36 wt% for $KTiH_3$, 2.22 wt% for $RbTiH_3$, and 1.65 wt% for $CsTiH_3$. Tahir et al. [31] explored $XSnH_3$ (X = K and Li) based simple cubic perovskites for hydrogen technology, reporting hydrogen densities between 1.88 and 2.35 wt%. Furthermore, numerous theoretical investigations have offered valuable understanding into the stability and physical characteristics of hydrides, emphasizing their potential for hydrogen storage i.e. K_2SnH_6 (2.48 wt%) [32], Rb_2GeH_6 (2.09 wt%) [32], $KNaMg_2H_6$ (5.19 wt %) [33], $Mg2FeH5$ (4.61 wt%) [13], Cs_2CaCdH_6 (1.39 wt %) [34], Rb_2CaCdH_6 (1.69 wt %) [34], Cs_2SrTlH_6 (1.61 wt %) [35], K_2LiGaH_6 (3.71 wt %) [36], Mg_2LiCuH_6 (4.83 wt %) [37], Ca_2LiCuH_6 (3.86 wt %) [37], and Sr_2LiCuH_6 (2.40 wt %) [37]. This research has greatly enhanced the understanding and advancement of double perovskite materials for efficient H_2 storage applications.

Motivated by findings from the literature review, this study utilized ab initio simulations to systematically and strategically design six novel solid-state double perovskite hydrides for hydrogen storage technologies. The structural, mechanical, thermodynamic, and optoelectronic properties, along with the hydrogen storage capabilities of Q_2LiMH_6 (Q = K, Rb; M = Ga, In, Tl), has been determined using a DFT approach on the basis of first principles calculation. To the best of our knowledge, the theoretical and experimental study of these features has not been undertaken before, making this study a pioneering effort in examining these double perovskites. The results of this research broaden the scope by providing a more comprehensive and detailed understanding of the significance of perovskites in advancing hydrogen technologies for various industrial applications.
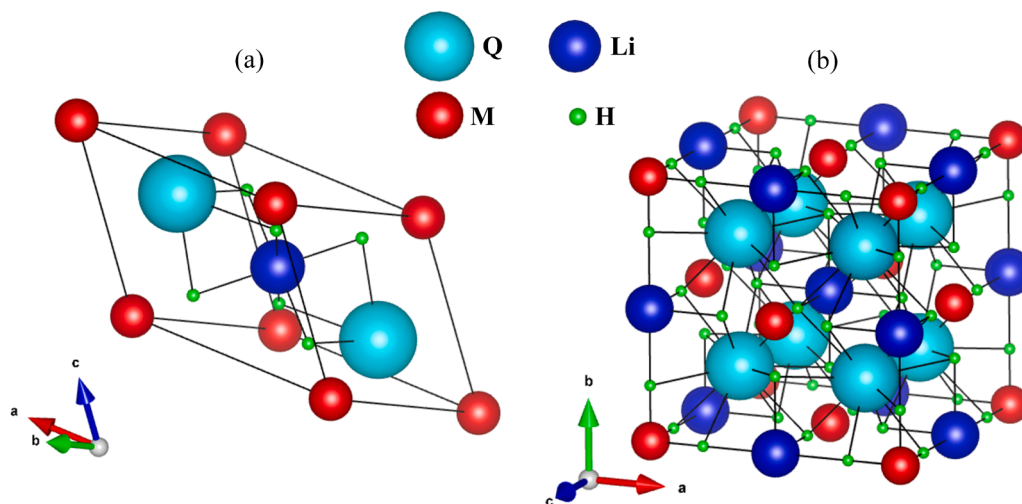

Fig. 1. Crystal structural representation of (a) the primitive and (b) the conventional unit cells of double perovskite hydrides (DPHs) Q_2LiMH_6 (Q = K, Rb; M = Ga, In, Tl) in the cubic phase, belonging to the $Fm\overline{3}m$ space group.
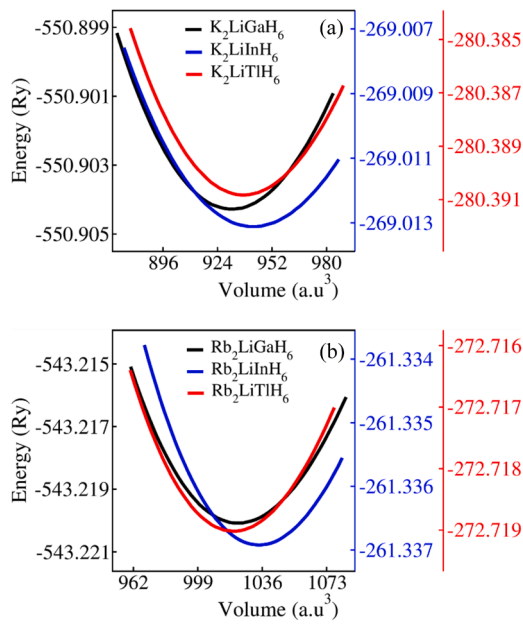
Fig. 2. Murnaghan fitted energy-volume graphs of Q_2LiMH_6 (Q = K, Rb; M = Ga, In, Tl) hydrides.

2. Computational analysis

The first principles calculations were conducted using Density functional theory (DFT), implemented in Quantum ESPRESSO (QE) [38], which is based on the projector augmented wave (PAW) method. For QE calculations, ultrasoft pseudopotentials from the Garrity− Bennett− Rabe− Vanderbilt (GBRV) library [39] was utilized to perform computations on single-cell unit of the perovskites. The Perdew–Burke–Ernzerhof (PBE) approximation within the generalized gradient approximation (GGA) [40,41] was applied to compute the exchange-correlation energy. Since the GGA functional typically underestimates band gap values, the HSE06 hybrid functional [42,43], recognized for its enhanced accuracy in electronic structure calculations, was also utilized in this study. The simulation study identified the most stable structures with minimal energy using the BFGS algorithm, and all subsequent calculations were conducted on these optimized configurations. The wavefunction cutoff was fixed at 70 Ry, with a charge density cutoff of 700 Ry, and the convergence threshold for self-consistent field (SCF) calculations was set to 10^{-8} Ry. Optical properties are determined using the real and imaginary parts of the dielectric function through the Kramers-Kronig relations [44]. The elastic constants and other mechanical properties of the Q_2LiMH_6 (Q = K, Rb; M = Ga, In, Tl) compounds were determined using the thermo_pw code [45], which utilizes the stress-strain approach. Phonon calculations were conducted using supercell and finite displacement methods, as implemented in the PHONOPY code [46]. A $2 \times 2 \times 2$ supercell of the primitive unit cell, comprising 80 atoms, was employed with an atomic displacement of 0.01 Å for generating the phonon dispersion curve of the hydrides. The crystal structure modeling and visualization were carried out using XCrySDen [47] and VESTA software [48].

3. Results and discussion

3.1. Structural and hydrogen storage properties

Theoretical models of the Q_2LiMH_6 (Q = K, Rb; M = Ga, In, Tl) double perovskite hydrides (DPHs) series suggest that these perovskite materials crystallize in the Fm$\overline{3}$m space group (No. 225), displaying a characteristic cubic structure. The crystal structure, both in its primitive and conventional forms, is displayed in Fig. 1a and b, respectively. The

Table 1
The optimized lattice parameters (*a*, Å), volume (*V*, Å³), bulk modulus (*B*, GPa), pressure derivative of bulk modulus (*B'*), minimum energy (E_0, Ry), formation energies (ΔH_E, Ry) and H_2 storage capacity ($C_{wt\%}$, wt%) of Q_2LiMH_6 (Q = K, Rb; M = Ga, In, Tl).

Materials	*a*	*V*	*B*	*B'*	E_0	ΔH_E	$C_{wt\%}$
K_2LiGaH_6	7.83	480.05	29.41	3.19	− 550.90	− 1.75	3.22
K_2LiInH_6	8.10	531.44	26.50	3.01	− 269.01	− 1.60	2.60
K_2LiTlH_6	8.21	553.39	25.72	3.33	− 280.39	− 0.79	1.88
Rb_2LiGaH_6	8.11	533.41	27.12	4.63	− 533.41	− 1.70	2.16
Rb_2LiInH_6	8.36	584.28	24.73	4.11	− 261.34	− 1.56	1.86
Rb_2LiTlH_6	8.45	603.35	23.94	4.65	− 272.72	− 0.76	1.46

unit cell of these hydrides comprises four formula units, totaling 40 atoms, with Q, Li, M, and H positioned at the Wyckoff sites 8c, 4b, 4a, and 24e, respectively. The structure can also be interpreted as a modified version of the ordered perovskite (ABX₃) structure, where the B sites are evenly shared by Li and M atoms. The isolated $[MH_6]^{3-}$ octahedra have hydrogen atoms directed toward the neighboring octahedral interstices, which are occupied by Li atoms. The Li atoms are likewise octahedrally coordinated by six hydrogen atoms, while the interstitial sites are fully occupied by Q atoms, which are 12-coordinated with hydrogen atoms.

Structural relaxation calculations for all six DPHs, including shape, volume, and ionic positions, are conducted at 0 K within the primitive unit cell. The optimized structures of the six perovskites are then utilized to determine static energies associated with the given static volumes. Afterward, we found E(V) curves as displayed in Fig. 2a & b through the third-order Birch-Murnaghan equation of state using Eq. (1) [49,50].

$$E(V) = E_0(V) + \frac{BV}{B'}\left[\frac{\left(\frac{V_0}{V}\right)^{B'}}{B' - 1} + 1\right] - \frac{BV_0}{B' - 1} \qquad (1)$$

In Eq. (1), E(V) represents the material's energy at a specific volume V, while E_0 denotes the total energy of the unit cell. B corresponds to the bulk modulus, V_0 is the equilibrium volume, and B' signifies the pressure derivative of the bulk modulus. The internal parameter value is determined by identifying the point where total energy convergence occurs. Table 1 presents a summary of the static and equilibrium structural properties at 0 K and 0 GPa. The smallest lattice constant is for K_2LiGaH_6 (7.83 Å), and the largest lattice constant is for Rb_2LiTlH_6 (8.45 Å). A rising trend in the lattice constant was noted, which is clearly attributed to the increasing atomic radii of the Q and M-site atoms. The unit cell volume follows a similar trend to that of the lattice constant; the calculated values can be found in Table 1. K_2LiGaH_6 appears to be the most stable among the compositions under study, owing to its higher ground-state energy ($E_0 = − 550.90$ Ry). Furthermore, the bulk modulus (B) values follow the order K_2LiGaH_6 > Rb_2LiGaH_6 > K_2LiInH_6 > K_2LiTlH_6 > Rb_2LiInH_6 > Rb_2LiTlH_6. With the highest bulk modulus, K_2LiGaH_6 is the most rigid compound among them.

The formation energies were calculated using Eq. (2), where E_{tot}^Q, E_{tot}^{Li}, E_{tot}^M, and $E_{tot}^{H_2}$ represent the ground state energies for one Q atom, one Li atom, one M atom, and one H atom, respectively. $E_{total}^{Q_2LiMH_6}$ refers to the optimized total energy of Q_2LiMH_6 compounds. The calculated formation energies are − 1.75 Ry for K_2LiGaH_6, − 1.60 Ry for K_2LiInH_6, − 0.79 Ry for K_2LiTlH_6, − 1.70 Ry for Rb_2LiGaH_6, − 1.56 Ry for Rb_2LiInH_6, and − 0.76 Ry for Rb_2LiTlH_6, suggesting that all the examined materials are thermodynamically stable and hold promise for feasible synthesis.

$$E_{form}^{Q_2LiMH_6} = E_{total}^{Q_2LiMH_6} - \left(2E_{tot}^Q + E_{tot}^{Li} + E_{tot}^M + 3E_{tot}^{H_2}\right) \qquad (2)$$

The gravimetric hydrogen storage capacity (GDH) of these compounds needs to be examined in order to evaluate their potential for application in hydrogen technology. It refers to the quantity of hydrogen
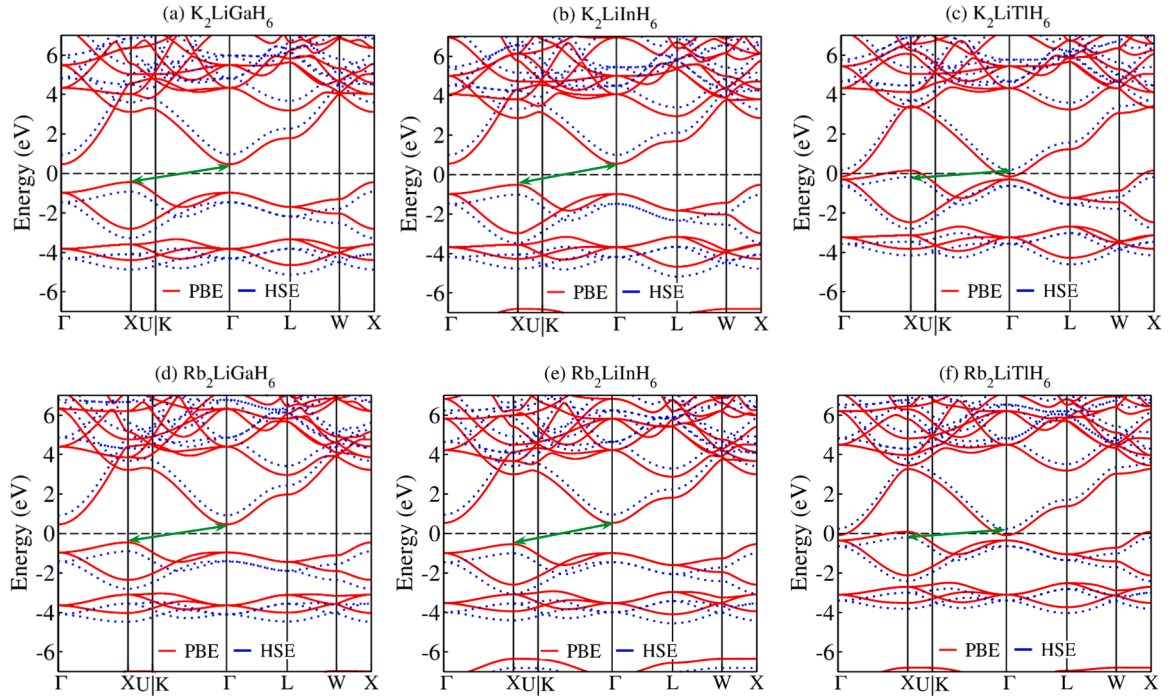
Fig. 3. The band structure of $Fm\overline{3}m$ Q_2LiMH_6 (Q = K, Rb; M = Ga, In, Tl) HDPs is shown for GGA (red) and HSE06 (blue dashed). High-symmetry points in the Brillouin zone are labeled according to the conventions specified in Refs. [73,74]. The horizontal black dotted line denotes the Fermi level (E_F).
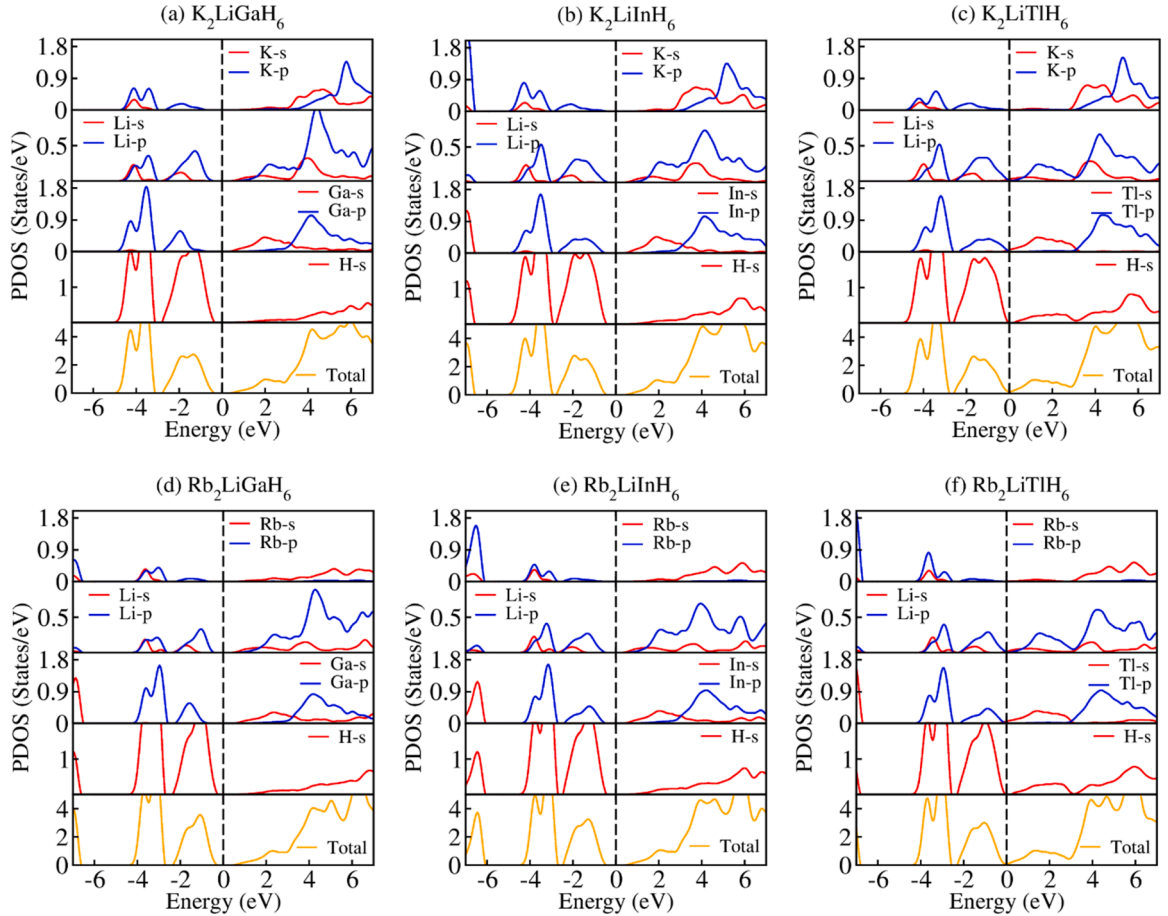

Fig. 4. TDOS and PDOS of double perovskite hydrides: (a) K_2LiGaH_6, (b) K_2LiInH_6, (c) K_2LiTlH_6, (d) Rb_2LiGaH_6, (e) Rb_2LiInH_6, and (f) Rb_2LiTlH_6. The vertical black dotted marker represents the Fermi level (E_F).
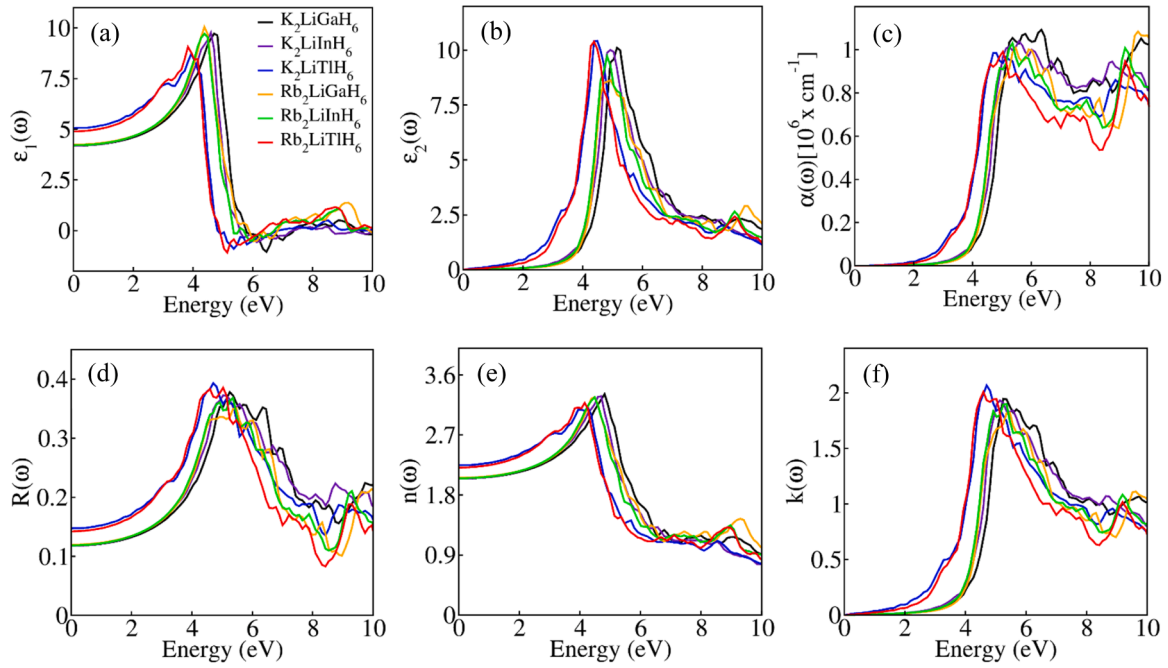
Fig. 5. Frequency-dependent (a & b) real and imaginary part of the dielectric function, ε(ω), (c) absorption coefficient α(ω) (in cm^{-1}), (d) reflectivity R(ω), (e) extinction coefficient k(ω), and (f) refractive index n(ω) for Q$_2$LiMH$_6$ (Q = K, Rb; M = Ga, In, Tl) hydrides.

that can be stored per unit weight of a given material. Table 1 presents the gravimetric hydrogen storage capacities of the analyzed perovskites, determined using Eq. (3).

$$C_{wt\%} = \left(\frac{\left(\frac{H}{M}\right) m_H}{m_{Host} + \left(\frac{H}{M}\right) m_H} \times 100 \right) \% \tag{3}$$

In Eq. (3), $\frac{H}{M}$ is the hydrogen to material atom ratio, m_H is the molar mass of hydrogen and m_{Host} denotes the molar mass of the host substance. Based on the computed gravimetric densities, it is determined that K$_2$LiGaH$_6$ has the highest GDH value of 3.22 wt%, followed by K$_2$LiInH$_6$ at 2.60%, Rb$_2$LiGaH$_6$ at 2.16%, K$_2$LiTlH$_6$ at 1.88%, Rb$_2$LiInH$_6$ at 1.86%, and Rb$_2$LiTlH$_6$ at 1.46%. When the Q and M atoms change from K to Rb and Ga to Tl, respectively, the GDH decreases due to the increase in the hydrides mass. Furthermore, the storage densities of these DPHs can be improved by using thin films and nanostructures with a larger surface area, offering greater storage potential in respect to their bulk counterparts [51].

3.2. Electronic properties

The electronic properties, including band structures and density of states (DOS), were determined across the high-symmetry directions within first Brillouin zone based on the optimized structural configurations of Q$_2$LiMH$_6$ (Q = K, Rb; M = Ga, In, Tl) DPHs. Two different approaches were employed for this calculation: GGA-PBE (represented by the red solid line) and the HSE06 hybrid functional (depicted by the blue dotted line), as shown in Fig. 3 (a–f). It is widely recognized that conventional approximations, like GGA-PBE, typically underestimate the band gap values by around 40% when compared to result of experiments [52,53]. In order to mitigate this limitation, the HSE06 approximation was utilized, providing more accurate predictions of band gaps. The band structure of the targeted six materials has been predicted across the high-symmetry paths of the first Brillouin zone (Γ− X− U|K− Γ− L− W− X), as illustrated in Fig. 3 (a–f). The obtained band gap (E$_g$) values using GGA-PBE (HSE06) approximations are 0.90 (1.88) eV for K$_2$LiGaH$_6$, 1.06 (1.98) eV for K$_2$LiInH$_6$, 0.00 (0.36) eV for

K$_2$LiTlH$_6$, 0.91 (1.87) eV for Rb$_2$LiGaH$_6$, 1.08 (1.97) eV for Rb$_2$LiInH$_6$, and 0.00 (0.49) eV for Rb$_2$LiTlH$_6$, respectively. Depicted in Fig. 3 (a–f), the HSE06 method increases the accuracy of the band gap while maintaining its nature unchanged compared to GGA-PBE. The GGA-PBE band structure of K$_2$LiTlH$_6$ and Rb$_2$LiTlH$_6$ exhibits no band gap, whereas the other four materials do. However, the HSE06 functional reveals that all DPHs have an indirect band gap, where the valence band maxima located at the X-point while conduction band minima at the Γ-point. Currently, there are no experimental results available regarding the E$_g$ values of these DPHs for direct comparison with our simulation results; however, based on prior experience with the HSE06 functional, we expect that these simulation findings will provide essential reference points for upcoming experimental research.

Furthermore, the total and partial DOS calculations offer a more comprehensive understanding of the band structure and the electronic contributions of the materials. Fig. 4 presents the PDOS and TDOS of Q$_2$LiMH$_6$ (Q = K, Rb; M = Ga, In, Tl) within the energy span from −7 to 7 eV. The DOS graphs illustrate the distinct roles of Q, Li, M and H atoms across different energy states. As plotted in Fig. 4 (a–f), the valence bands of the perovskites, spanning −7 eV to 0 eV, are primarily influenced from H-*s*, and *p*-states of Q, Li, and M. On the contrary, within the energy spanning 0 eV to 7 eV, the conduction bands, are primarily occupied with *s*-states of Q, Li and M atoms, along with a minor role from H-*s* and Li-*p* orbitals. The above determined E$_g$ values can be validated through analyzing TDOS of Q$_2$LiMH$_6$ as revealed in Fig. 4 (a–f).

3.3. Optical properties

Analyzing the optical behavior of solids is essential for understanding how they respond to incident photons. The complex dielectric function (DF), ε(ω), quantifies how a solid reacts to an external electromagnetic (EM) field across varying frequencies (ω) and comprises two components: ε$_1$(ω) and ε$_2$(ω), as follows:

$$\varepsilon(\omega) = \varepsilon_1(\omega) + i\varepsilon_2(\omega) \tag{4}$$

The real and imaginary portions of DF can be expressed by ε$_1$(ω) and ε$_2$(ω), respectively. These components can be determined using specific

equations:

$$\varepsilon_1(\omega) = 1 + \frac{2}{\pi} P \int_0^\infty \frac{\omega'^{\varepsilon_2}(\omega')}{\omega'^2 - \omega^2} d\omega' \qquad (5)$$

P is the Cauchy integral.

$$\varepsilon_2(\omega) = \frac{(4\pi^2 e^2)}{(\pi\omega^2 m^2)} \sum_{ij} \int_{BZ} \left[M_{ij}(k) \right]^2 f_i \left(1 - f_j \right) \delta \left[E_f - E_i - \omega \right] d^3 k \qquad (6)$$

In the formulae, M_{ij} (k) represents the dipole matrix.

DF also has a direct relationship with the other optical parameters, covering absorption coefficient $\alpha(\omega)$, reflectance $R(\omega)$, refractive index n(ω), and extinction coefficient k(ω). These properties are determined using the equations provided below:

$$\alpha(\omega) = \sqrt{2}\omega \left[-\varepsilon_1(\omega) + \sqrt{\varepsilon_1^2(\omega) + \varepsilon_2^2(\omega)} \right]^{1/2} \qquad (7)$$

$$R(\omega) = \left| \frac{\sqrt{\varepsilon(\omega)} - 1}{\sqrt{\varepsilon(\omega)} + 1} \right|^2 \qquad (8)$$

$$n(\omega) = \left[\frac{\sqrt{\varepsilon_1^2(\omega) + \varepsilon_2^2(\omega)} + \varepsilon_1(\omega)}{2} \right]^{\frac{1}{2}} \qquad (9)$$

$$k(\omega) = \left[\frac{\sqrt{\varepsilon_1^2(\omega) + \varepsilon_2^2(\omega)} - \varepsilon_1(\omega)}{2} \right]^{\frac{1}{2}} \qquad (10)$$

Fig. 5(a) illustrates the real components of DF for Q_2LiMH_6 (Q = K, Rb; M = Ga, In, Tl) hydrides. The static DF $\varepsilon_1(0)$ of K_2LiGaH_6, K_2LiInH_6, K_2LiTlH_6, Rb_2LiGaH_6, Rb_2LiInH_6, and Rb_2LiTlH_6 are 4.18, 4.19, 5.05, 4.24, 4.21, and 4.89 respectively. Furthermore, the peak values of $\varepsilon_1(\omega)$ for K_2LiGaH_6, K_2LiInH_6, K_2LiTlH_6, Rb_2LiGaH_6, Rb_2LiInH_6, and Rb_2LiTlH_6 are 9.73 (at 4.74 eV), 9.80 (at 4.63 eV), 8.73 (at 3.98 eV), 10.12 (at 4.40 eV), 9.73 (at 4.38 eV), and 9.09 (at 3.85 eV), respectively. The presence of some negative values for these HDPs suggests limited transmission and optical loss at a specific photon energy [54,55]. Additionally, $\varepsilon_1(\omega)$ of DF may become negative once the frequency of the imposed EM field surpasses the plasma frequency of the substance. Consequently, the electrons are not able to interact efficiently with the external electric field, leading the substance to behave as an ideal reflector [56]. In Fig. 5(b), $\varepsilon_2(\omega)$ of DF for Q_2LiMH_6 (Q = K, Rb; M = Ga, In, Tl) initially rises and then declines as energy increases within the lower energy range. The peak values for the hydrides K_2LiGaH_6, K_2LiInH_6, K_2LiTlH_6, Rb_2LiGaH_6, Rb_2LiInH_6, and Rb_2LiTlH_6 in the X axis are recorded as 10.14 at 5.15 eV, 9.99 at 4.95 eV, 10.39 at 4.50 eV, 8.60 at 4.94 eV, 9.84 at 4.81 eV, and 10.39 at 4.41 eV, respectively.

The absorption coefficient $\alpha(\omega)$, indicates the extent to which a material absorbs incident light at its surface. Fig. 5(c) demonstrates the absorption spectra for the studied materials, showing their variation in relation to photon energy. The absorption edges for all hydrides are initially zero at zero incident photon energy and then appear at energy corresponding to the respective E_g values. Also, all materials exhibit no significant peak within visible range; instead, they appear in the ultraviolet area, indicating their role as UV absorbers. The K_2LiGaH_6 compound exhibits the highest absorption rate of 1.10×10^6 cm^{-1} at 6.37 eV, surpassing other hydrides within ultraviolet spectrum. The reflectivity $R(\omega)$ is determined using Eq. (8), which determines how effectively a material reflects incoming light and is strongly affected by its electronic properties [57]. As shown in Fig. 5d, K_2LiTlH_6 demonstrates the highest reflectivity, reaching 40% at 4.72 eV, indicating strong light reflection in this range. The static reflectance at zero eV of K_2LiGaH_6, K_2LiInH_6, K_2LiTlH_6, Rb_2LiGaH_6, Rb_2LiInH_6, and Rb_2LiTlH_6 are 0.118,

Table 2
Elastic constant (C_{ij}, GPa) of Q_2LiMH_6 (Q = K, Rb; M = Ga, In, Tl).

Materials	C_{11}	C_{12}	C_{44}
K_2LiGaH_6	59.92	19.81	38.91
K_2LiInH_6	48.41	12.89	31.37
K_2LiTlH_6	36.67	17.65	28.43
Rb_2LiGaH_6	55.54	21.01	37.29
Rb_2LiInH_6	44.45	12.56	31.38
Rb_2LiTlH_6	43.97	21.91	28.85

0.117, 0.147, 0.12, 0.118, and 0.142 accordingly.

The extinction coefficient k(ω) serves as an essential fundamental parameter that quantifies a material's ability to intake EM radiation at specific frequencies [58]. It is the imaginary part of the refractive index n(ω), characterizes how an electromagnetic wave propagates and attenuates within a solid [59]. It is evident that the extinction coefficient k(ω) shows a similar trend to $\varepsilon_2(\omega)$, while the refractive index n(ω) aligns with the variation of $\varepsilon_1(\omega)$ with respect to photon energies, as depicted in Fig. 5a & b. The value of n(ω = 0) exceeding 1 indicates that the speed of light in the examined perovskites is reduced compared to its speed in a vacuum [60]. Notably, the peaks of n(ω) for all hydrides fall in the range of 4 eV to 6 eV, with K_2LiTlH_6 showing the maximum peak value around 4.72 eV, while Rb_2LiTlH_6, K_2LiGaH_6, K_2LiInH_6, Rb_2LiInH_6, and Rb_2Li-GaH_6 display progressively lower peaks.

3.4. Elastic and mechanical properties

Elastic constants (ECs) serve as crucial elements in comprehending the way crystals respond to applied stress, offering insight into the solid's mechanical characteristics [29]. The strength and stability of a material can be assessed by measuring these ECs. All six hydrides possess a cubic lattice arrangement, which are characterized with three elastic constants − C_{11}, C_{12}, and C_{44} − employed to evaluate mechanical stability based on Born's criterion. Table 2 indicates that the elastic constants of Q_2LiMH_6 (Q = K, Rb; M = Ga, In, Tl) satisfy the Born-Huang criterion [61] in Eq. (11) for cubic crystals. Therefore, all six materials satisfy the requirements for mechanical stability as per the Born criteria and exhibit excellent stability during hydrogenation and dehydrogenation processes.

$$C_{11} > 0, \; C_{11} - C_{12} > 0, \; C_{11} + 2C_{12} > 0 \text{ and } C_{11} > B_0 > C_{12} \qquad (11)$$

C_{11} signifies the material's capacity to resist deformation under longitudinal stress, C_{12} reflects the response to transverse strain, whereas C_{44} expresses to material's hardness, particularly in terms of shear deformation under an external load. Table 2 illustrates the C_{11} values for the analyzed double perovskites are ordered as follows: K_2LiGaH_6 > Rb_2LiGaH_6 > K_2LiInH_6 > Rb_2LiInH_6 > Rb_2LiTlH_6 > K_2LiTlH_6. The elastic constant C_{11} value is highest for K_2LiGaH_6 (59.92 GPa) and lowest for K_2LiTlH_6 (36.67 GPa). This indicates that K_2LiGaH_6 possesses the greatest resistance to longitudinal deformation, making it the hardest among the studied materials, whereas K_2LiTlH_6 is comparatively soft due to its minimal resistance to longitudinal deformation.

The estimated ECs values for crystalline materials enable the calculation of elastic moduli, which define various mechanical properties of polycrystalline compounds. The elastic moduli, including bulk modulus (B), shear modulus (G), Young's modulus and Poisson's ratio v, has been determined using the Voigt-Reuss-Hill (VRH) assumptions by utilizing the following relations:

$$B = B_v = B_R = \frac{(C_{11} + 2C_{12})}{3} \qquad (12)$$

Table 3
Mechanical attributes of Q$_2$LiMH$_6$ (Q = K, Rb; M = Ga, In, Tl).

Materials	B	G	E	$C_p = C_{12} - C_{44}$	ν	B/G	A
K$_2$LiGaH$_6$	33.18	29.82	68.81	− 19.10	0.154	1.112	1.940
K$_2$LiInH$_6$	24.73	24.97	56.03	− 18.48	0.122	0.990	1.766
K$_2$LiTlH$_6$	23.99	18.35	43.73	− 10.78	0.192	1.307	2.989
Rb$_2$LiGaH$_6$	32.52	27.37	64.07	− 16.28	0.171	1.188	2.159
Rb$_2$LiInH$_6$	23.19	23.91	53.36	− 18.82	0.116	0.969	1.968
Rb$_2$LiTlH$_6$	29.27	19.62	48.03	− 6.94	0.224	1.491	2.615

$$B_H = \frac{(B_R + B_v)}{2} \tag{13}$$

$$G_v = \frac{C_{11} - C_{12} + 3C_{44}}{5} \tag{14}$$

$$G_R = \frac{5C_{44}(C_{11} - C_{12})}{4C_{44} + 3(C_{11} - C_{12})} \tag{15}$$

$$G_H = \frac{(G_R + G_v)}{2} \tag{16}$$

Afterward, the young modulus (Y), and Poisson's ratio (ν) were determined utilizing Hill's approximations for the shear and bulk moduli.

$$Y = \frac{9BG}{3B + G} \tag{17}$$

$$\nu = \frac{3B - 2G}{2(3B + G)} \tag{18}$$

The bulk modulus (B) reflects a material's ability to resist compression when pressure is applied. As presented in Table 3, K$_2$LiGaH$_6$ exhibits the highest B value, indicating its superior resistance to compression. Conversely, Rb$_2$LiInH$_6$ possesses the minimal B value, indicating that it is the highly compressible of the analyzed perovskites. The shear modulus (G) represents a substance's opposition to deformation under shear force. As observed in Table 3, K$_2$LiGaH$_6$ exhibits the highest G values compared to the other materials studied, which aligns with the obtained B values. Young's modulus (E) measures the stiffness of a solid material. Its value was calculated using Eq. (17), and the outcomes are presented within Table 3. It was observed that K$_2$LiGaH$_6$ (68.81 GPa) exhibits the maximum Y value, followed by Rb$_2$LiGaH$_6$ (64.07 GPa), K$_2$LiInH$_6$ (56.03 GPa), Rb$_2$LiInH$_6$ (53.36 GPa), Rb$_2$LiTlH$_6$ (48.03 GPa), and K$_2$LiTlH$_6$ (43.73 GPa) which has the lowest value. However, as far as the author is aware, no relevant data is available in the literature for comparison.

A more detailed evaluation of whether a perovskite exhibits ductile or brittle behavior can be examined utilizing three parameters: Pugh's criteria (B/G ratio), Poisson's ratio (ν), and Cauchy pressure (C$_p$). Cauchy pressure (C$_p$), defined as the difference between C$_{11}$ and C$_{44}$, acts as a measure of a substance's mechanical properties— a positive result suggests a ductile nature, whereas a negative result implies a brittle characteristic. As displayed in Table 3, the negative C$_p$ results demonstrate that all the studied hydrides exhibit brittle behavior. Based on Frantsevich et al.'s [62] criterion for Poisson's ratio, a compound is considered ductile if $\nu > 0.26$, whereas brittle if $\nu < 0.26$. The calculated Poisson's ratio for Q$_2$LiMH$_6$ is less than 0.26, indicating that these materials display a tendency toward brittleness, as shown in Table 3. Another essential parameter is the Pugh ratio (B/G), which acts as a key indicator for distinguishing between brittle and ductile characteristics in a substance. Materials with a B/G ratio of less than 1.75 are classified as brittle, while those with a B/G ratio exceeding 1.75 demonstrate ductility. In this study, all the compounds analyzed show brittleness with B/G ratios below 1.75, consistent with Poisson's ratio and Cauchy pressure results.

In various technological applications, the anisotropic nature of crystal structures plays a crucial role, significantly influencing key
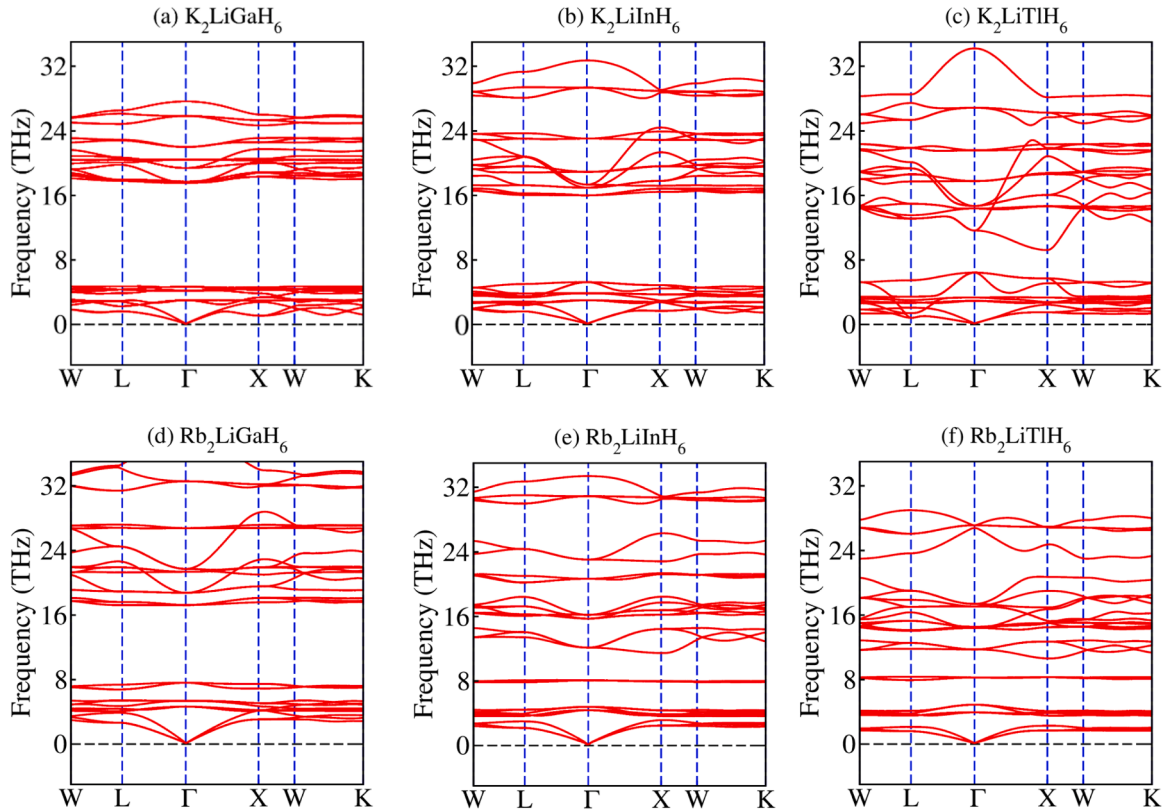

Fig. 6. The phonon dispersion curves of (a) K$_2$LiGaH$_6$, (b) K$_2$LiInH$_6$, (c) K$_2$LiTlH$_6$, (d) Rb$_2$LiGaH$_6$, (e) Rb$_2$LiInH$_6$, and (f) Rb$_2$LiTlH$_6$.
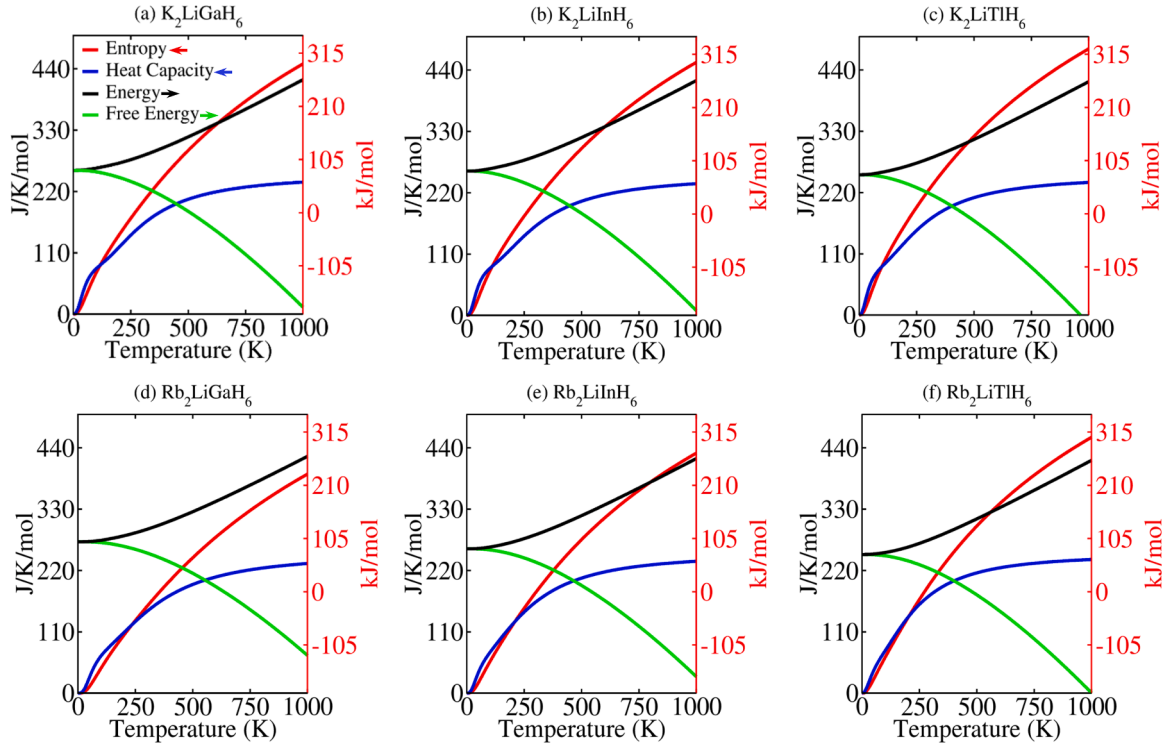
Fig. 7. Variation of entropy, constant heat capacity, energy and free energy in relation to temperature curves for Q_2LiMH_6 (Q = K, Rb; M = Ga, In, Tl) hydrides.

phenomena like phonon modes and plastic deformation [63]. Moreover, the anisotropy factor (A) serves as crucial indicator for understanding the extent of anisotropy in a material. A deviation of the anisotropy factor (A) from one indicates an anisotropic system, while a value equal to one signifies isotropy. The anisotropic factor of the materials was calculated using Eq. (19), revealing anisotropic behavior consistent with findings reported for similar materials in existing literature [34–37].

$$A = \frac{2C_{44}}{C_{11} - C_{12}} \tag{19}$$

3.5. Vibrational and thermodynamic properties

Phonon dispersion analysis is essential for evaluating the structural stability of crystals and understanding how vibrational modes influence thermodynamic behavior [64]. Currently, no experimental data is available on the acoustic characteristics of double perovskite hydrides Q_2LiMH_6 (Q = K, Rb; M = Ga, In, Tl). Thus, determining the phonon stability of these hydrides through computational analysis, such as DFT, is crucial. The $2 \times 2 \times 2$ supercells generated for six compounds were utilized in Quantum Espresso, and the phonon dispersion graphs have been determined utilizing the linear response approach. As illustrated in Fig. 6(a–f), the absence of negative frequencies throughout the Brillouin region, especially at the gamma-point, verifies the dynamic stability for all the analyzed hydride materials. Dynamically stable materials typically enable cyclic hydrogen absorption, allowing repeated hydrogen storage and release while reducing degradation or performance loss [65]. Notably, the maximum phonon frequencies for K_2LiGaH_6, K_2LiInH_6, K_2LiTlH_6, Rb_2LiGaH_6, Rb_2LiInH_6, and Rb_2LiTlH_6 are found to be 27.67 THz, 32.57 THz, 34.18 THz, 37.98 THz, 33.48 THz, and 29.14 THz, respectively. As highlighted in previous studies [66,67], hydrogen, as the least dense constituent in the materials, contributes to elevated frequencies, whereas the lower frequencies are primarily governed by the heavier atoms K, Rb, Ga, In and Tl.

Afterward, utilizing processed phonon information along with utilizing the quasi-harmonic Debye framework, the thermodynamic pa-

rameters of cubic Q_2LiMH_6 (Q = K, Rb; M = Ga, In, Tl) HDPs have been calculated, encompassing entropy (S), heat capacity (C_v), energy (E), and free energy (F) [68]. The equations based on the quasi-harmonic Debye model are presented below:

$$S(T) = k_B \left\{ \int \frac{\hbar\omega/k_BT}{\exp(\hbar\omega/k_BT) - 1} F(\omega) \, d\omega - \int F(\omega) \ln[1 - \exp(-\hbar\omega/k_BT)] \, d\omega \right\} \tag{20}$$

$$C_V(T) = k_B \int \frac{(\hbar\omega/k_BT)^2 \exp(\hbar\omega/k_BT)}{[\exp(\hbar\omega/k_BT) - 1]^2} F(\omega) \, d\omega \tag{21}$$

$$E(T) = E_{tot} + E_{zp} + \int \frac{\hbar\omega}{\exp(\hbar\omega/k_BT)} F(\omega) \, d\omega \tag{22}$$

$$F(T) = E_{tot} + E_{zp} + k_BT \int F(\omega) \ln[1 - \exp(-\hbar\omega/k_BT)] \, d\omega \tag{23}$$

In the given equation, k_B stands for the Boltzmann constant, while $\hbar$ represents Planck's constant. The function $F(\omega)$ corresponds to the phonon density of states, and T denotes the temperature of the Q_2LiMH_6 hydrides. Furthermore, E_{tot} and E_{zp} refer to the total energy and zero-point energy of these hydrides, respectively. Fig. 7(a–f) display the trends in thermodynamic parameters within the 0–1000 K temperature span. The thermodynamic properties for all six studied materials exhibit a similar overall trend. Entropy provides information about the level of randomness within a crystal and, as temperature increases, thermal vibrations intensify, leading to greater disorder within the system [66]. As shown in the entropy plot in Fig. 7, when temperature nears its minimal possible value (0 K), its internal energy drops substantially. It indicates that upon reaching zero temperature, entropy almost disappears, in harmony with the 3rd law of thermodynamics, denoting an exceptionally organized crystal system within all hydrides [69,70]. The influence of temperature variations on the vibrational contributions to the specific heat capacities (C_v) for all compounds has been analyzed and presented in Fig. 7. The plot reveals a rapid increase in C_v up to approximately 600 K, followed by a plateau, indicating the onset of the Dulong-Petit limit
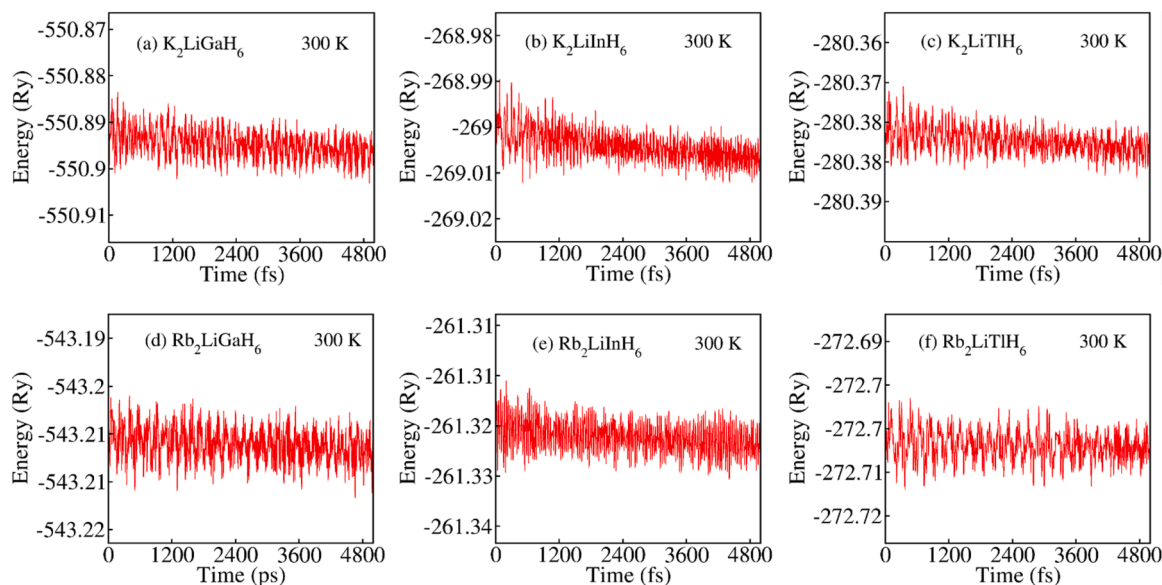
Fig. 8. Total energy fluctuation at 300 K estimated in ab initio molecular dynamic (AIMD) simulations of Q_2LiMH_6 (Q = K, Rb; M = Ga, In, Tl) hydrides.

[71]. Below 650 K, the specific heat capacities of compounds vary significantly with temperature and approach zero at 0 K. Furthermore, our observations indicate that for all six hydrides, the energy curves increase, whereas the free energy curves decrease as the temperature rises.

3.6. Molecular dynamic simulation

AIMD investigations gas been performed at room temperature (300 K) for the cubic hydride Q_2LiMH_6 (Q = K, Rb; M = Ga, In, Tl), maintaining this temperature for a duration of 5 ps (5000 fs). The robustness of these double perovskites was assessed through the analysis of fluctuations in total energy in relation to time. A system is considered thermally stable and structurally ordered if the total energy exhibits only minor fluctuations around a constant value [72]. As shown in Fig. 8 (a-f), the energy profiles of all hydrides indicate that they remain relatively stable throughout the 5 ps simulation, exhibiting only slight fluctuations. Consequently, this discussion draws the outcome that Q_2LiMH_6 hydrides exhibit thermal stability. These insights improve our understanding of these hydrides behavior in real-world applications, especially in contexts where thermal stability is essential for hydrogen storage systems and other energy-related advancements.

4. Conclusion

This research investigates the hydrogen storage capabilities and physical characteristics of six newly designed double perovskite hydrides, Q_2LiMH_6 (Q = K, Rb; M = Ga, In, Tl), through first-principles calculations. The structural stability of the compounds was first evaluated through geometry optimization. The resulting crystal structures exhibited a stable cubic configuration, with lattice constants of 7.83 Å, 8.10 Å, 8.21 Å, 8.11 Å, 8.36 Å, and 8.45 Å for K_2LiGaH_6, K_2LiInH_6, K_2LiTlH_6, Rb_2LiGaH_6, Rb_2LiInH_6, and Rb_2LiTlH_6, respectively. The exchange-correlation effects were considered utilizing the GGA and HSE06 approximations. The band structure analysis confirmed that all the investigated compounds exhibit semiconducting behavior with an indirect band gap. The optical characteristics of these hydrides suggest that they possess high efficiency in UV energy absorption. The brittle nature of these compounds has been predominantly identified through the analysis of Cauchy pressure, Poisson's ratio, and the B/G ratio. Also, K_2LiGaH_6 is identified to be the hardest substance within the examined DPHs. Various thermodynamic parameters, including free energy,

enthalpy, entropy, and heat capacity, are calculated in relation to functions of temperature and the findings reveal that enthalpy along with entropy rises as temperature elevates, whereas free energy declines. The gravimetric hydrogen densities (GDH) are 3.22 wt% for K_2LiGaH_6, 2.60 wt% for K_2LiInH_6, 2.16 wt% for Rb_2LiGaH_6, 1.88 wt% for K_2LiTlH_6, 1.86 wt% for Rb_2LiInH_6, and 1.46 wt% for Rb_2LiTlH_6. K_2LiGaH_6 exhibits outstanding H_2 storage potential within the investigated materials, making it a promising option in the field of H_2 technologies. Unfortunately, no existing reference data is available for comparison. As far as the author's understanding goes, this research represents the first comprehensive theoretical investigation of these double perovskite hydrides. Thus, this study serves as a valuable foundation for next-generation theoretical and experimental research and comparisons.

CRediT authorship contribution statement

Asif Hosen: Writing – review & editing, Writing – original draft, Visualization, Validation, Software, Resources, Methodology, Investigation, Conceptualization. **Ahmad A. Mousa:** Writing – review & editing, Writing – original draft, Investigation. **Ebrahim Nemati-Kande:** Writing – review & editing, Software. **Asif Nawaz Khan:** Writing – review & editing, Software, Data curation. **Mohammed S. Abu-Jafar:** Formal analysis, Data curation. **Enrico Benassi:** Validation, Investigation, Writing – original draft, Writing – review & editing. **E.A. Elghmaz:** Writing – review & editing, Funding acquisition, Data curation. **N.S. Abd EL-Gawaad:** Writing – review & editing, Resources, Funding acquisition, Writing – original draft. **Jihad Asad:** Resources, Formal analysis, Data curation.

Declaration of competing interest

The authors declare that they have no known competing financial interests or personal relationships that could have appeared to influence the work reported in this paper.

Data availability

Data will be made available on request.

References

[1] J. Ran, J. Zhang, J. Yu, M. Jaroniec, S.Z. Qiao, Earth-abundant cocatalysts for semiconductor-based photocatalytic water splitting, Chem. Soc. Rev. 43 (2014) 7787–7812.

[2] M.G. Rasul, M.A. Hazrat, M.A. Sattar, M.I. Jahirul, M.J. Shearer, The future of hydrogen: challenges on production, storage and applications, Energy Convers. Manage 272 (2022) 116326, https://doi.org/10.1016/j.enconman.2022.116326.

[3] N. Fajrina, M. Tahir, A critical review in strategies to improve photocatalytic water splitting towards hydrogen production, Int. J. Hydrog. Energy 44 (2019) 540–577, https://doi.org/10.1016/j.ijhydene.2018.10.200.

[4] J. Van Mierlo, G. Maggetto, P. Lataire, Which energy source for road transport in the future? A comparison of battery, hybrid and fuel cell vehicles, Energy Convers. Manage. 47 (2006) 2748–2760.

[5] G. Marbán, T. Valdés-Solís, Towards the hydrogen economy? Int. J. Hydrog. Energy 32 (2007) 1625–1637.

[6] R. Shinnar, The hydrogen economy, fuel cells, and electric cars, Technol. Soc. 25 (2003) 455–476.

[7] M. Granovskii, I. Dincer, M.A. Rosen, Economic and environmental comparison of conventional, hybrid, electric and hydrogen fuel cell vehicles, J. Power. Sources. 159 (2006) 1186–1193.

[8] L.Z. Ouyang, H.W. Dong, C.H. Peng, L.X. Sun, M. Zhu, A new type of Mg-based metal hydride with promising hydrogen storage properties, Int. J. Hydrog. Energy 32 (2007) 3929–3935.

[9] K. Ikeda, Y. Kogure, Y. Nakamori, S. Orimo, Formation region and hydrogen storage abilities of perovskite-type hydrides, Progr. Solid State Chem. 35 (2007) 329–337.

[10] P. Chen, X. Wu, J. Lin, K.L. Tan, High H2 uptake by alkali-doped carbon nanotubes under ambient pressure and moderate temperatures, Science 285 (1999) (1979) 91–93.

[11] A. Dillon, K.M. Jones, T.A. Bekkedahl, C.H. Kiang, D.S. Bethune, M.J. Heben, Storage of hydrogen in single-walled carbon nanotubes, Nature 386 (1997) 377–379.

[12] H. Imamura, K. Masanari, M. Kusuhara, H. Katsumoto, T. Sumi, Y. Sakata, High hydrogen storage capacity of nanosized magnesium synthesized by high energy ball-milling, J. Alloys. Compd. 386 (2005) 211–216.

[13] A. Hosen, D. Dahliah, N.F.A. Mohammad, A.A. Mousa, M.S. Abu-Jafar, A computational study on the comparative analysis of tetragonal complex metal hydride Q2FeH5 (Q= Mg, Ca, Sr) for hydrogen storage applications, Int. J. Hydrog. Energy 102 (2025) 348–359.

[14] P. Chen, Z. Xiong, J. Luo, J. Lin, K.L. Tan, Interaction of hydrogen with metal nitrides and imides, Nature 420 (2002) 302–304.

[15] S. Niaz, T. Manzoor, A.H. Pandith, Hydrogen storage: materials, methods and perspectives, Renew. Sustain. Energy Rev.50 (2015) 457–469. https://doi.org/10.1016/j.rser.2015.05.011.

[16] N.A.A. Rusman, M. Dahari, A review on the current progress of metal hydrides material for solid-state hydrogen storage applications, Int. J. Hydrog. Energy 41 (2016) 12108–12126.

[17] D. Sun, S.S. Srinivasan, G. Chen, C.M. Jensen, Rehydrogenation and cycling studies of dehydrogenated NaAlH4, J. Alloys. Compd. 373 (2004) 265–269.

[18] T. Vegge, Equilibrium structure and Ti-catalyzed H 2 desorption in NaAlH 4 nanoparticles from density functional theory, Phys. Chem. Chem. Phys. 8 (2006) 4853–4861.

[19] F. Schüth, B. Bogdanović, M. Felderhoff, Light metal hydrides and complex hydrides for hydrogen storage, Chem. Commun. (2004) 2249–2258.

[20] B. Bogdanović, U. Eberle, M. Felderhoff, F. Schüth, Complex aluminum hydrides, Scr. Mater. 56 (2007) 813–816.

[21] G. Sandrock, J. Reilly, J. Graetz, W.-M. Zhou, J. Johnson, J. Wegrzyn, Accelerated thermal decomposition of AlH3 for hydrogen-fueled vehicles, Appl. Phys. A 80 (2005) 687–690.

[22] K. Chłopek, C. Frommen, A. Léon, O. Zabara, M. Fichtner, Synthesis and properties of magnesium tetrahydroborate, Mg (BH4) 2, J. Mater. Chem. 17 (2007) 3496–3503.

[23] M.L. Christian, K.-F. Aguey-Zinsou, Core–shell strategy leading to high reversible hydrogen storage capacity for NaBH4, ACS Nano 6 (2012) 7739–7751.

[24] S. Niaz, T. Manzoor, A.H. Pandith, Hydrogen storage: materials, methods and perspectives, Renew. Sustain. Energy Rev. 50 (2015) 457–469.

[25] B. Sakintuna, F. Lamari-Darkrim, M. Hirscher, Metal hydride materials for solid hydrogen storage: a review, Int. J. Hydrog. Energy 32 (2007) 1121–1140.

[26] R.J. Farrauto, Catalysts for the hydrogen economy, Prepr. Pap. Am. Chem. Soc. Div. Fuel. Chem 48 (2003) 685.

[27] S. Orimo, H. Fujii, Materials science of Mg-Ni-based new hydrides, Appl. Phys. A 72 (2001) 167–186.

[28] T. Sato, H. Blomqvist, D. Noréus, Attempts to improve Mg2Ni hydrogen storage by aluminium addition, J. Alloys Compd. 356 (2003) 494–496.

[29] H. Naeem, M.A. Ullah, A. Hussain, Y. Sandali, Z. Usman, M. Rizwan, Exploring novel characteristics of GaBaX3 (X= F, Cl, Br, I, H) for energy harvesting applications: A DFT-based analysis, Int. J. Hydrog. Energy 105 (2025) 203–213.

[30] N. Xu, Y. Chen, S. Chen, S. Li, W. Zhang, First-principles investigation for the hydrogen storage properties of XTiH3 (X= K, Rb, Cs) perovskite type hydrides, Int. J. Hydrog. Energy 50 (2024) 114–122.

[31] M. Tahir, M. Usman, J.U. Rehman, M.B. Tahir, A first-principles study to investigate the physical properties of Sn-based hydride perovskites XSnH3 (X= K, Li) for hydrogen storage application, Int. J. Hydrog. Energy 50 (2024) 845–853.

[32] Q. Dai, T.-Y. Tang, Q.-Q. Liang, Z.-Q. Chen, Y. Wang, Y.-L. Tang, Exploration of A2BH6(A = K, Rb; B = Ge, Sn) hydrides for hydrogen storage applications: A first principles study, Int. J. Hydrog. Energy 92 (2024) 769–778, https://doi.org/10.1016/j.ijhydene.2024.10.324.

[33] T. Tang, Y. Tang, First-principles investigations for the structural, optoelectronic and hydrogen storage properties of double perovskite KNaMg2F6-xHx and KNaAe2H6(Ae=Be, Mg, Ca), Int. J. Hydrog. Energy 61 (2024) 13–24, https://doi.org/10.1016/j.ijhydene.2024.02.237.

[34] W. Azeem, S. Hussain, M.K. Shahzad, F. Azad, G. Khan, V. Tirth, H. Alqahtani, A. Alghtani, T. Al-Mughanam, Y.H. Wong, Computational insights of double perovskite X2CaCdH6 (X= Rb and Cs) hydride materials for hydrogen storage applications: a DFT analysis, Int. J. Hydrog. Energy 79 (2024) 514–524.

[35] M. Shafqat Hayat, R.M.A. Khalil, Ab-initio exploration of unique and substantial computational properties of double hydrides Cs2CaTlH6, Cs2SrTlH6, & Cs2BaTlH6, for the computational manufacturing of hydrogen fuel cell: A DFT study, J. Mol. Graph. Model. 125 (2023) 108600, https://doi.org/10.1016/j.jmgm.2023.108600.

[36] Q. Dai, T.-Y. Tang, Z.-Q. Chen, Y. Wang, Y.-L. Tang, A DFT study to investigate of K2LiXH6 (X= Al, Ga, In) perovskite hydrides for hydrogen storage application, Int. J. Hydrog. Energy 101 (2025) 295–302.

[37] A. Ayyaz, M.A. Ullah, M. Zaman, N.D. Alkhaldi, Q. Mahmood, I. Boukhris, M.S. Al-Buriahi, M. mana Al-Anazy, Investigation of hydrogen storage and energy harvesting potential of double perovskite hydrides A2LiCuH6 (A= Be/Mg/Ca/Sr): A DFT approach, Int. J. Hydrog. Energy 102 (2025) 1329–1339.

[38] P. Giannozzi, S. Baroni, N. Bonini, M. Calandra, R. Car, C. Cavazzoni, D. Ceresoli, G.L. Chiarotti, M. Cococcioni, I. Dabo, QUANTUM ESPRESSO: a modular and open-source software project for quantum simulations of materials, J. Phys. 21 (2009) 395502.

[39] K.F. Garrity, J.W. Bennett, K.M. Rabe, D. Vanderbilt, Pseudopotentials for high-throughput DFT calculations, Comput. Mater. Sci. 81 (2014) 446–452.

[40] J.P. Perdew, K. Burke, M. Ernzerhof, Generalized gradient approximation made simple, Phys. Rev. Lett. 77 (1996) 3865.

[41] J.P. Perdew, Orbital functional for exchange and correlation: self-interaction correction to the local density approximation, Chem. Phys. Lett. 64 (1979) 127–130.

[42] J. Heyd, G.E. Scuseria, Efficient hybrid density functional calculations in solids: assessment of the Heyd–Scuseria–Ernzerhof screened Coulomb hybrid functional, J. Chem. Phys. 121 (2004) 1187–1192.

[43] J. Heyd, G.E. Scuseria, M. Ernzerhof, Hybrid functionals based on a screened coulomb potential, J. Chem. Phys. 118 (2003) 8207–8215.

[44] F.T. Geldasa, F.B. Dejene, M.A. Kebede, F.G. Hone, E.T. Jira, Density functional theory study of chlorine, fluorine, nitrogen, and sulfur doped rutile TiO2 for photocatalytic application, Sci. Rep. 15 (2025) 3390.

[45] A. Dal Corso, Elastic constants of beryllium: a first-principles investigation, J. Phys. 28 (2016) 075401.

[46] A. Togo, I. Tanaka, First principles phonon calculations in materials science, Scr. Mater. 108 (2015) 1–5, https://doi.org/10.1016/j.scriptamat.2015.07.021.

[47] A. Kokalj, XCrySDen—A new program for displaying crystalline structures and electron densities, J. Mol. Graph. Model. 17 (1999) 176–179.

[48] K. Momma, F. Izumi, VESTA 3 for three-dimensional visualization of crystal, volumetric and morphology data, J. Appl. Crystallogr. 44 (2011) 1272–1276.

[49] F.D. Murnaghan, The compressibility of media under extreme pressures, Proc. Natl. Acad. Sci. 30 (1944) 244–247.

[50] F. Birch, Finite elastic strain of cubic crystals, Phys. Rev. 71 (1947) 809.

[51] D.P. Broom, C.J. Webb, G.S. Fanourgakis, G.E. Froudakis, P.N. Trikalitis, M. Hirscher, Concepts for improving hydrogen storage in nanoporous materials, Int. J. Hydrog. Energy 44 (2019) 7768–7779.

[52] T. Saadi, H. Baaziz, T. Ghellab, H. Latelli, A. Telfah, Z. Charifi, Electronic structure, mechanical and optical properties of hydrogen storage alkaline amides XNH₂ (X= Li, Na) compounds, Int. J. Hydrog. Energy 102 (2025) 1480–1496.

[53] E. Engel, S.H. Vosko, Exact exchange-only potentials and the virial relation as microscopic criteria for generalized gradient approximations, Phys. Rev. B 47 (1993) 13164.

[54] R.N. Singh, N.H. March, Intermetallic Compounds–Principle and Practice, John Wiley and Sons, Chichester, UK, 1995, p. 195.

[55] N. Al-Zoubi, A. Almahmoud, A. Almahmoud, A. Obeidat, Theoretical assessment of a novel NaXH3 and KXH3 (X= Tc, Ru and Rh) perovskite hydrides for hydrogen storage, Int. J. Hydrog. Energy 93 (2024) 822–831.

[56] C. Kittel, P. McEuen, Introduction to Solid State Physics, John Wiley & Sons, 2018.

[57] M.U. Ghani, M. Sagir, M.B. Tahir, H.I. Elsaeedy, S. Nazir, H. Alrobei, M. Alzaid, CASTEP investigation of structural, electronic, and optical properties of halide perovskites RbXCl3 (X= Ge, Sn, Pb) for solar cell applications, Inorg. Chem. Commun. 155 (2023) 111007.

[58] O. Hakami, H.J. Alathlawi, Study of mechanical, optoelectronic, and thermoelectric characteristics of Be/Mg ions based double perovskites A2FeH6 (A= Be, Mg) for hydrogen storage applications, Int. J. Hydrog. Energy 83 (2024) 307–316.

[59] M. Nabi, D.C. Gupta, Potential lead-free small band gap halide double perovskites Cs2CuMCl6 (M= Sb, Bi) for green technology, Sci. Rep. 11 (2021) 12945.

[60] N. Al-Zoubi, A. Almahmoud, A. Almahmoud, A. Obeidat, Theoretical assessment of a novel NaXH3 and KXH3 (X= Tc, Ru and Rh) perovskite hydrides for hydrogen storage, Int. J. Hydrog. Energy 93 (2024) 822–831.

[61] M. Born, K. Huang, Dynamical Theory of Crystal Lattices, Oxford University Press, 1996.

[62] I.N. Frantsevich, Elastic Constants and Elastic Moduli of Metals and Insulators, Reference Book, 1982.

[63] V. Tvergaard, J.W. Hutchinson, Microcracking in ceramics induced by thermal expansion or elastic anisotropy, J. Am. Ceram. Soc. 71 (1988) 157–166.

[64] T. Saadi, H. Baaziz, T. Ghellab, H. Latelli, A. Telfah, Z. Charifi, Electronic structure, mechanical and optical properties of hydrogen storage alkaline amides XNH₂ (X= Li, Na) compounds, Int. J. Hydrog. Energy 102 (2025) 1480–1496.

[65] J. Zhang, D. Zhou, J. Liu, First-principles investigation of Mg2CoH5 complex hydride, Trans. Nonferr. Metals Soc. China 19 (2009) 205–209.

[66] N. Xu, R. Song, J. Zhang, Y. Chen, S. Chen, S. Li, Z. Jiang, W. Zhang, First-principles study on hydrogen storage properties of the new hydride perovskite XAlH3 (X= Na, K), Int. J. Hydrog. Energy 60 (2024) 434–440.

[67] A. Gencer, G. Surucu, Investigation of structural, electronic and lattice dynamical properties of XNiH3 (X= Li, Na and K) perovskite type hydrides and their hydrogen storage applications, Int. J. Hydrog. Energy 44 (2019) 15173–15182.

[68] H.L. Chen, L. Lin, P.L. Mao, Z. Liu, Phase stability, electronic, elastic and thermodynamic properties of Al-RE intermetallics in Mg-Al-RE alloy: A first principles study, J. Magn. Alloys 3 (2015) 197–202.

[69] V. Shukla, A. Bhatnagar, S.K. Verma, A.P. Pandey, A.K. Vishwakarma, P. Srivastava, T.P. Yadav, O.N. Srivastava, Simultaneous improvement of kinetics and thermodynamics based on SrF2 and SrF2@ gr additives on hydrogen sorption in MgH2, Mater. Adv. 2 (2021) 4277–4290.

[70] G.P. Johari, Entropy, enthalpy and volume of perfect crystals at limiting high pressure and the third law of thermodynamics, Thermochim. Acta 698 (2021) 178891.

[71] E.I. Andritsos, E. Zarkadoula, A.E. Phillips, M.T. Dove, C.J. Walker, V.V Brazhkin, K. Trachenko, The heat capacity of matter beyond the Dulong–Petit value, J. Phys. 25 (2013) 235401.

[72] G.M. Mustafa, B. Younas, H.D. Alkhaldi, A. Mera, A.K. Alqorashi, J. Hakami, S. A. Mahmoud, I. Boukhris, Q. Mahmood, First principle study of physical aspects and hydrogen storage capacity of magnesium-based double perovskite hydrides Mg2XH6 (X= Cr, Mn), Int. J. Hydrog. Energy 95 (2024) 300–308.

[73] Y. Hinuma, G. Pizzi, Y. Kumagai, F. Oba, I. Tanaka, Band structure diagram paths based on crystallography, Comput. Mater. Sci. 128 (2017) 140–184.

[74] M.I. Aroyo, D. Orobengoa, G. de la Flor, E.S. Tasci, J.M. Perez-Mato, H. Wondratschek, Brillouin-zone database on the Bilbao Crystallographic Server, Acta Crystallogr. A 70 (2014) 126–137.